Assessing the reconstruction of the critical line in the QCD phase diagram from imaginary to real chemical potential

Fabrizio Murgana[*] and Marco Ruggieri[†]

Department of Physics and Astronomy "Ettore Majorana," University of Catania, Via Santa Sofia 64, I-95123 Catania, Italy and INFN-Sezione di Catania, Via Santa Sofia 64, I-95123 Catania, Italy

(Received 12 May 2025; accepted 19 July 2025; published 8 September 2025)

We test a technique adopted in the lattice simulations framework, to reconstruct the chiral-phase boundary at real chemical potential, μ, via extrapolation from imaginary μ. We use a low-energy effective model, the quark-meson model, both in the mean-field approximation and within the functional renormalization group, the latter in the local potential approximation. The model provides results both for real and imaginary values of μ; thus a direct comparison can be performed between the prediction of the model for real values of μ and the ones obtained via extrapolation from the results at imaginary μ. We compute an effective convergence radius for the reconstruction technique, $\mu_{\rm conv}$, and find $\mu_{\rm conv} \approx 263$ MeV. This value sustains the validity of the reconstruction technique also for finite and moderate values of the chemical potential. On the other hand, within our model, $\mu_{\rm conv}$ is smaller then the value of μ where we find the actual critical endpoint. Near this point of the phase diagram, we find a discrepancy between the actual phase boundary and the one obtained via extrapolation of $\approx$100%. Therefore, our results show that the location of the critical endpoint obtained via reconstruction from imaginary μ might be considered with due caution.

DOI: 10.1103/vl7y-j84r

I. INTRODUCTION

The study of quantum chromodynamics (QCD) under extreme conditions of temperature and baryon density remains one of the central challenges in contemporary physics. Of particular interest is the behavior of strongly interacting matter at finite temperature and chemical potential, as it governs the phase structure of QCD, including the possible existence of a critical endpoint (CEP) separating regions of crossover and first-order phase transition [1–8]. This complex landscape is not only of theoretical significance but also directly relevant to experimental programs in heavy-ion collisions, where the search for signals of the QCD phase transition and the CEP constitutes a major objective [9–12].

In this context, lattice QCD provides a first-principles framework for calculating the thermodynamics of QCD. At vanishing chemical potential, μ, lattice simulations are firmly established and have produced highly accurate results for quantities such as the equation of state, fluctuations of conserved charges, and correlation functions [13–15]. However, as the baryon chemical potential increases, lattice QCD calculations are hindered by the well-known sign problem, which severely restricts direct simulations in the high-density regime [16]. This challenge has motivated the development of various indirect reconstruction techniques—such as Taylor expansions [17,18], analytic continuation from imaginary chemical potential [19,20], and complex Langevin methods [21,22] to extend lattice results to finite chemical potential.

Parallel to these efforts, a wide array of effective models has been developed to explore the thermodynamics of QCD in regions where lattice calculations become intractable. Models such as the Nambu–Jona-Lasinio model [23,24], quark-meson models [25,26], Polyakov-loop extended chiral models [27], and others attempt to capture essential features of QCD by incorporating key symmetries and interactions, often calibrated to reproduce lattice data at zero or low chemical potential. While these models lack the first-principles rigor of lattice QCD, they are invaluable tools for exploring qualitative trends, making predictions at high baryon density, and testing scenarios for the structure of the QCD phase diagram.

The main purpose of our work is to perform a comparative analysis between the reconstruction of the critical boundary via continuation of the results from imaginary to real μ, and the actual boundary computed at real μ. In particular, we want to check whether the continuation of the

[*]Contact author: fabrizio.murgana@dfa.unict.it
[†]Contact author: marco.ruggieri@dfa.unict.it

Published by the American Physical Society under the terms of the Creative Commons Attribution 4.0 International license. Further distribution of this work must maintain attribution to the author(s) and the published article's title, journal citation, and DOI. Funded by SCOAP[3].

critical line from imaginary to real μ gives, within our model, a reasonable estimate of the location of the CEP at real μ. A similar study within the Dyson-Schwinger equation framework can be found in [28]. By examining the phase diagram predicted by the model at both real and imaginary μ, we assess the degree to which the reconstruction aligns with model predictions, and how this agreement evolves as one approaches the CEP. Such a comparison serves multiple purposes: in fact, it validates the reconstruction technique in the small μ region, and identifies the limitations of the reconstruction as μ is increased and the CEP is approached.

Specifically, we exploit the quark-meson (QM) model [25,26,29,30] both in the mean-field (MF) and in the hydrodynamical formulation of the functional renormalization group (FRG) in the local potential approximation (LPA) scheme. This technique has previously been applied to various effective models and for calculations at real μ up to the critical endpoint (see, e.g., [5,31–35]). In the present work, we extend its application to imaginary μ. By performing calculations at imaginary μ, then following a similar extrapolation procedure as employed in lattice QCD studies, we compare the extrapolated crossover transition line with the results obtained explicitly through our functional approach.

Our results demonstrate a clear and systematic trend. At low μ, the reconstructed critical line and the actual one exhibit a high degree of agreement, consistent with the expectation that both approaches are well grounded in this regime. However, as μ increases and approaches the region associated with the CEP, the agreement begins to falter. The increasing discrepancy reflects the growing influence of critical fluctuations and nonperturbative dynamics that are challenging to capture by a simple extrapolation of the results at imaginary μ. Thus, our findings can serve as a benchmark for assessing the reliability of the extrapolation method commonly adopted in the lattice framework.

This article is organized as follows. In Sec. II, we describe the quark meson model as an effective low-energy description of chiral symmetry breaking in QCD. Section III provides an overview of the theoretical FRG setup used in this study. Section IV presents the comparative analysis of the results, with particular attention to the behavior of key observables as functions of chemical potential. Finally, in Sec. V, we summarize our findings and discuss their implications for future work on the QCD phase diagram and the search for the critical endpoint.

II. MODEL SETUP

The QM model provides an effective framework to describe low-energy QCD, extending the linear sigma model by incorporating fermionic degrees of freedom [25,26,30]. In the case of two quark flavors ($N_f = 2$), the fundamental fields of the QM model include an isospin triplet of pions, $\vec{\pi} = (\pi_1, \pi_2, \pi_3)$, and a scalar isosinglet field, σ. These mesonic fields couple to a massless isospin doublet fermion field, ψ, which represents the up and down quarks. The Euclidean Lagrangian density for this model is given by

$$\mathcal{L}_{\mathrm{E}}^{\mathrm{QM}} = \bar{\psi}[\gamma_\mu \partial_\mu + h(\sigma + i\gamma_5 \vec{\tau}\cdot\vec{\pi})]\psi \tag{1}$$

$$+\frac{1}{2}(\partial_\mu \sigma)^2 + \frac{1}{2}(\partial_\mu \vec{\pi})^2 + U(\sigma^2 + \vec{\pi}^2) - c\sigma, \tag{2}$$

where γ_μ and γ_5 are the Euclidean Dirac matrices, h denotes the Yukawa coupling constant controlling the interaction between quarks and mesons, and $\vec{\tau} = (\tau^1, \tau^2, \tau^3)$ represents the Pauli matrices in flavor space. The potential $U(\sigma^2 + \vec{\pi}^2)$ is designed to maintain $O(4)$ symmetry, as it depends solely on the invariant combination $\sigma^2 + \vec{\pi}^2$. However, if the potential acquires a minimum in a particular direction, spontaneous symmetry breaking occurs, reducing $O(4)$ to $O(3)$. This symmetry breaking allows one to choose a vacuum configuration in which

$$\langle \vec{\pi} \rangle = 0, \qquad \langle \sigma \rangle = f_\pi \neq 0, \tag{3}$$

where $f_\pi = 0.093$ GeV corresponds to the pion decay constant.

Although the Lagrangian does not include an explicit mass term for the quarks, spontaneous symmetry breaking generates a dynamical mass for them, given by

$$M = h\langle \sigma \rangle. \tag{4}$$

Moreover, the term $-c\sigma$ explicitly breaks $O(4)$ symmetry, effectively mimicking the presence of a small but finite current quark mass. Owing to this explicit symmetry breaking, the pions acquire a finite mass, behaving as pseudo-Goldstone bosons. Their mass is given by

$$M_\pi^2 = \frac{c}{f_\pi}. \tag{5}$$

III. FUNCTIONAL RENORMALIZATION GROUP FRAMEWORK

In this section, we provide a concise overview of the FRG approach, following the formulation introduced by Wetterich and collaborators [36–39]. For a more detailed discussion, the reader is referred to Refs. [33,40–43].

The central quantity in this framework is the effective action, $\Gamma[\Phi]$, which serves as the generator of one-particle irreducible vertex functions. To facilitate its computation, an intermediate quantity known as the effective average action, $\bar{\Gamma}_k[\Phi]$, is introduced. This function depends on a momentumlike parameter k, which acts as a coarse-graining scale. The evolution of $\bar{\Gamma}_k[\Phi]$ is described by the FRG flow equation, governing its transition from the

ultraviolet (UV) regime ($k \to \infty$) to the infrared (IR) limit ($k \to 0$). The effective average action smoothly interpolates between the bare classical action, $S_{\text{bare}}[\Phi]$, at high energies and the full quantum effective action, $\Gamma[\Phi]$, in the low-energy limit:

$$\bar{\Gamma}_{k\to\infty}[\Phi] = S_{\text{bare}}[\Phi], \qquad \bar{\Gamma}_{k\to 0}[\Phi] = \Gamma[\Phi]. \tag{6}$$

In practical applications, it is not always feasible to take $k \to \infty$. Instead, a finite UV cutoff Λ is introduced as the initial scale for the FRG flow. This cutoff is chosen to be significantly larger than any other physical scale in the theory to ensure that the bare classical action accurately describes the system at this energy scale. However, since using a finite cutoff introduces an approximation, it is crucial to verify that physical results remain independent of Λ, which can be achieved by maintaining renormalization group consistency (see, for example, [34]).

The evolution of $\bar{\Gamma}_k[\Phi]$ as fluctuations with decreasing momenta are integrated out is described by the Wetterich equation, also known as the exact renormalization group equation [37,44]

$$\partial_k \bar{\Gamma}_k[\Phi] = \mathrm{Tr}\left[\frac{1}{2}\partial_k R_k (\bar{\Gamma}_k^{(2)}[\Phi] + R_k)^{-1}\right]. \tag{7}$$

Here, the trace represents a summation over all internal degrees of freedom as well as an integration over momenta. This equation exhibits a one-loop structure since it contains the full propagator, which is given by

$$G_k[\Phi] = (\bar{\Gamma}_k^{(2)}[\Phi] + R_k)^{-1}, \tag{8}$$

where R_k is the regulator function. The regulator R_k is chosen to ensure a smooth transition between the bare action and the full effective action, imposing that R_k should act as a mass term for low-momentum modes ($p < k$), regularizing the propagator in the IR, and vanish in the limit $k \to 0$ so that the full quantum effective action is recovered. Furthermore R_k should diverge as $k \to \infty$ to ensure that the functional integral defining $\bar{\Gamma}_k[\Phi]$ is dominated by the bare action at high energies.

The precise form of R_k is problem dependent and can be optimized according to various criteria [45–48]. Although the Wetterich equation appears compact, it is a functional integro-differential equation and cannot be solved exactly in general. To make progress, approximations must be introduced. Two widely used approaches are the vertex expansion [38,49,50] and the derivative expansion [43,51]: in the vertex expansion, $\bar{\Gamma}_k[\Phi]$ is expanded in powers of the fields, with the expansion coefficients given by the n-point vertex functions

$$\bar{\Gamma}_k^{(n)}(x_1, \ldots, x_n) = \left.\frac{\delta^n \bar{\Gamma}_k[\Phi]}{\delta\Phi(x_1)\cdots\delta\Phi(x_n)}\right|_{\Phi=\Phi_0}. \tag{9}$$

In the derivative expansion, $\bar{\Gamma}_k[\Phi]$ is expressed as a series of composite operators involving derivatives of the fields. These terms must respect the symmetries of the theory.

Both expansions lead to an infinite hierarchy of coupled integro-differential equations, which must be truncated at a given order. In this work, we focus on the derivative expansion, as it remains valid even near phase transitions, where nonanalyticities may arise in the effective action. In contrast, the vertex expansion assumes regularity of $\bar{\Gamma}_k[\Phi]$, which can break down at critical points due to singularities or discontinuities in the FRG flow (see, e.g., [5,31,33,35,52,53]).

Retaining the full advantage of the properties of the derivative expansion, we adopt the lowest-order truncation, commonly referred to as the LPA [43,45,54]. In this work, we apply the LPA ansatz to the QM model at finite temperature and nonzero quark chemical potential, which leads to the effective action

$$\begin{aligned}\Gamma_k[\bar{\psi},\psi,\phi] = &\int_0^\beta dx_4 \int d^3x \bar{\psi}[\gamma^\mu\partial_\mu + h(\sigma + i\gamma_5\vec{\tau}\cdot\vec{\pi}) - \mu\gamma^0]\psi \\ &+ \int_0^\beta dx_4 \int d^3x \left[\frac{1}{2}(\partial_\mu\sigma)^2 + \frac{1}{2}(\partial_\mu\vec{\pi})^2 + U_k(\sigma^2+\vec{\pi}^2) - c\sigma\right].\end{aligned} \tag{10}$$

To regulate the flow equations, we employ the three-dimensional Litim regulator [55,56], applied separately to bosons and fermions, namely,

$$R_{k,B}(p) = (k^2 - p^2)\Theta(k^2 - p^2), \tag{11}$$

$$R_{k,F}(p) = i\not{p}\left(\frac{k^2}{p^2} - 1\right)\Theta(k^2 - p^2). \tag{12}$$

Here, the subscripts B and F denote boson and fermion regulators respectively. Using this regulator, the flow equation for the effective potential reads as

$$\partial_t U_k(\sigma) = -\frac{k^5}{12\pi^2}\left\{\left[\frac{1}{E_{k,\sigma}}\coth\left(\frac{E_{k,\sigma}}{2T}\right)+\frac{3}{E_{k,\pi}}\coth\left(\frac{E_{k,\pi}}{2T}\right)\right]+\frac{4N_c}{E_\psi}\left[\tanh\left(\frac{E_\psi-\mu}{2T}\right)+\tanh\left(\frac{E_\psi+\mu}{2T}\right)\right]\right\}. \quad (13)$$

Here, $t=-\ln(k/\Lambda)$, while the energy terms are defined as

$$E_{k,\sigma}=\sqrt{k^2+\partial_\sigma^2 U_k(\sigma)}, \quad (14)$$

$$E_{k,\pi}=\sqrt{k^2+\frac{\partial_\sigma U_k(\sigma)}{\sigma}}, \quad (15)$$

$$E_\psi=\sqrt{p^2+M^2}, \quad (16)$$

and the constituent quark mass is given by $M=h\langle\sigma\rangle$.

We now follow the prescription given in previous works (see, e.g., [31,33,52,57,58]) and define

$$u_k(\sigma)=\partial_\sigma U_k(\sigma), \quad (17)$$

$$u_k'(\sigma)=\partial_\sigma u_k(\sigma). \quad (18)$$

Taking the derivative of the flow equation with respect to σ, we obtain an advection-diffusion equation with a source term [5,53,58]:

$$\partial_t u_k(\sigma)+\partial_\sigma f_k(\sigma,u_k(\sigma))=\partial_\sigma g_k(u_k'(\sigma))+N_c\partial_\sigma S_k(\sigma), \quad (19)$$

where the different contributions are defined as follows. Firstly, the advection flux is

$$f_k(\sigma,u_k(\sigma))=\frac{k^5}{4\pi^2}\frac{1}{E_{k,\pi}}\coth\left(\frac{E_{k,\pi}}{2T}\right). \quad (20)$$

The next contribution is the diffusion flux,

$$g_k(u_k'(\sigma))=-\frac{k^5}{12\pi^2}\frac{1}{E_{k,\sigma}}\coth\left(\frac{E_{k,\sigma}}{2T}\right). \quad (21)$$

Finally, the source term is

$$N_c S_k(\sigma)=\frac{N_c k^5}{3\pi^2}\frac{1}{E_\psi}\left[\tanh\left(\frac{E_\psi-\mu}{2T}\right)+\tanh\left(\frac{E_\psi+\mu}{2T}\right)\right]. \quad (22)$$

Within this framework, the function $u_k(\sigma)$ plays the role of a conserved quantity, as it obeys a generalized conservation law (see, e.g., [59–62] for a general review on the topic, and [58,63–65] for FRG applications). Each term in the equation originates from a different physical process. The advection flux arises from the pion sector. The presence of the factor of 3 in Eq. (5) confirms this contribution. Since the pion mass term $u_k(\sigma)/\sigma$ vanishes at the minimum of the effective potential, pions behave as Goldstone bosons. Furthermore, the characteristic speed $\partial_u f_k(\sigma,u_k(\sigma))$ is positive for $\sigma<0$ and negative for $\sigma>0$, meaning that $u_k(\sigma)$ and the minimum of the potential are advected toward lower values of σ. The diffusion term is induced by the radial sigma mode and depends on the curvature $u_k'(\sigma)$. Diffusion acts to smooth out gradients in $u_k(\sigma)$, thereby suppressing sharp features and discontinuities. Finally, the source term arises from the fermionic loop, leading to a time- and σ-dependent modification of the flow equation. Unlike the other contributions, this term is independent of $u_k(\sigma)$ itself, reinforcing its role as an external source.

As a final comment, we point out that the standard MF approximation can be formally recovered from Eq. (13) and Eq. (19) by properly rescaling the flow equation and taking the $N_c\to\infty$ limit.

IV. RESULTS

In this section, we present the results obtained both in the mean field and in the FRG formulation. The pseudocritical phase boundary within the model can be easily obtained by locating the pseudocritical temperature, for a fixed either real or imaginary chemical potential, via the peak of

$$\chi_\sigma=-\frac{\partial\sigma}{\partial T}, \quad (23)$$

where σ indicates the expectation value of the sigma field obtained as the position of the minimum of the effective potential. In correspondence with a real second-order phase transition χ_σ diverges; thus we identify the pseudocritical temperature as the location of the peak of χ_σ as a function of temperature. The resulting phase boundaries, obtained both in the MF and FRG formulations of the QM model are depicted in Fig. 3.

In Fig. 1 we plot σ versus temperature for $\mu=0$ (solid line), $\mu=0.2$ GeV (dot-dashed line), and then $i\mu=0.1$, 0.2 GeV (dot-dot-dashed and dashed line respectively). The upper panel corresponds to the results obtained within the MF approximation, while in the lower panel we show the results obtained within the FRG scheme. As expected, for a given value of the chemical potential, increasing temperature results in the lowering of σ. We can identify a temperature range in which the lowering of σ is more pronounced. This allows us to define the pseudocritical temperature by looking at the maximum of χ_σ defined in Eq. (23). Increasing μ along the real axis, the pseudocritical temperature decreases. On the other hand, increasing μ along the imaginary axis results in the increase of the

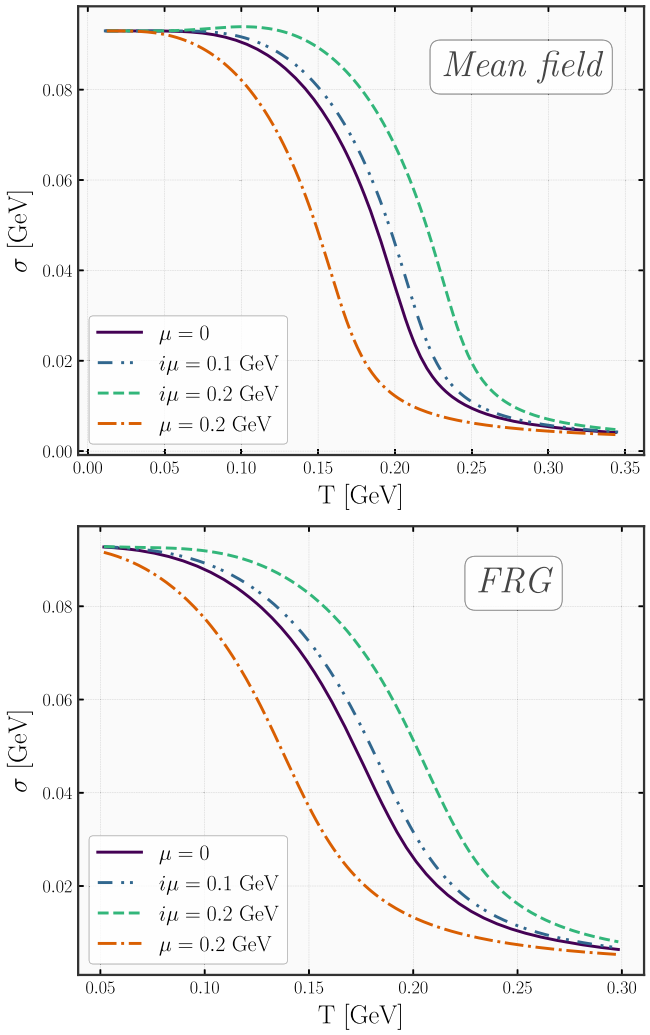


FIG. 1. Expectation value of the σ field as a function of temperature T for different imaginary and real values of the chemical potential μ in the MF case (upper panel) and in the FRG case (lower panel).

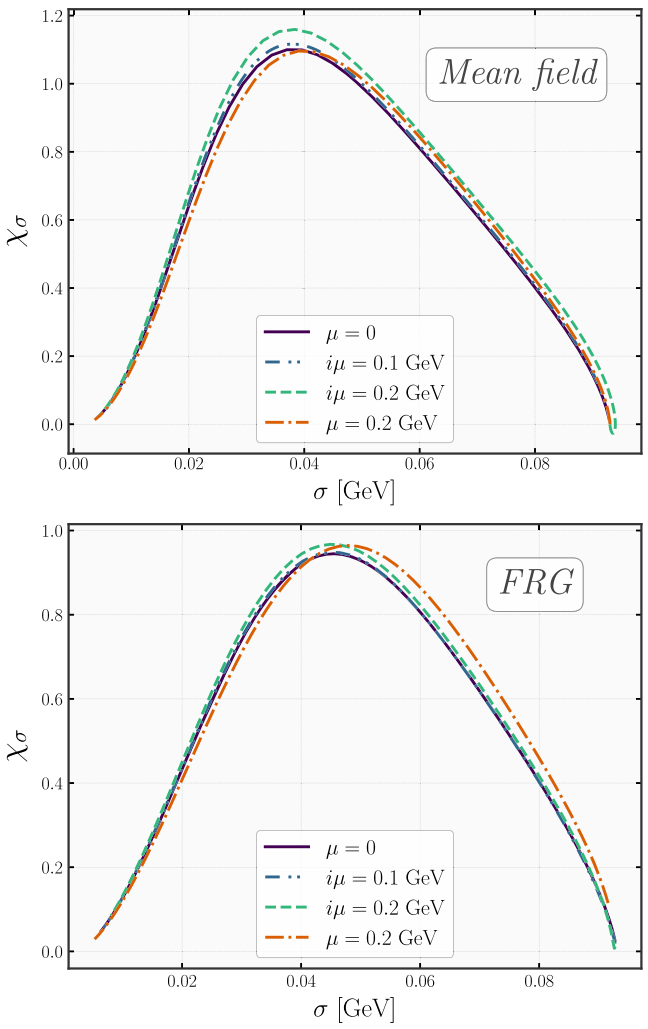


FIG. 2. χ_σ as a function of the expectation value of the σ field for different imaginary and real values of the chemical potential μ in the MF case (upper panel) and in the FRG case (lower panel).

critical temperature. The behavior of σ for the latter case that we have found is in agreement with previous results; see, for example, [66].

Our analysis on the pseudocritical temperature at fixed chemical potential is completed with the results shown in Fig. 2, where we plot χ_σ versus σ. The upper and lower panels correspond to results obtained within MF approximation and FRG scheme respectively. In order to compile the data in Fig. 2, for a given value of μ, σ is computed at a temperature via minimization of the effective potential; then χ_σ is computed at the same temperature. This figure is analogous to Fig. 2 of [28]. The behavior of χ_σ versus σ allows us to identify the temperature at which χ_σ has its maximum.

Next we focus on the pseudocritical line. Our main purpose is to compare the results obtained through extrapolation from imaginary to real chemical potential, with those directly obtained by the model computations.

In Fig. 3, we display the pseudocritical temperature derived at both imaginary and real chemical potentials. The results have been obtained by looking at the location of the maxima of χ_σ as explained above. The blue dots denote results from model computations; the dashed black line corresponds to the Roberge-Weiss (RW) limit. The solid line corresponds to a numerical fit of $T_c(\mu)$ with the standard functional form [20,67]:

$$\frac{T_c(\mu)}{T_c} = 1 - \kappa_2\left(\frac{\mu}{T_c}\right)^2 - \kappa_4\left(\frac{\mu}{T_c}\right)^4, \tag{24}$$

where $T_c = T_c(\mu = 0)$, κ_2 and κ_4 quantify the curvature and the kurtosis of the phase boundary. We remark that in the literature, these coefficients are usually computed using the baryon chemical potential $\mu_b = 3\mu$ instead μ. This implies that they have to be adjusted in case one is interested in a quantitative comparison with other studies.

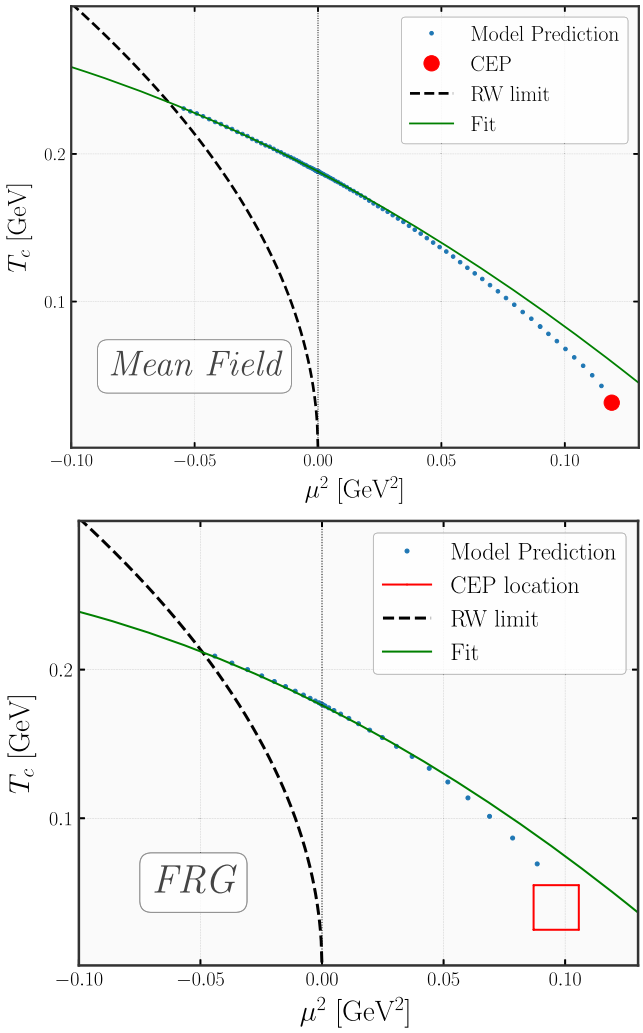


FIG. 3. Phase boundary of the QM model in the mean field approximation (upper panel) and in the FRG case (lower panel), for both real and imaginary chemical potential μ. The blue dots indicate the model prediction while the continuous green line indicates the reconstruction obtained via the techniques adopted in the lattice quantum chromodynamics framework based on imaginary chemical potential results. The red dot in the upper panel indicates the location of the CEP predicted by the model, while in the lower panel the red box includes also the uncertainties on its location due to the backbending phenomenon.

For the purpose of the present study however, this difference is irrelevant. For completeness, we collect the parameters κ_2 and κ_4 in Table I for MF and FRG calculations.

Since in the model calculations we have access to the critical temperature both for real and imaginary chemical potential, we can compare the actual results obtained for T_c at real μ with those obtained by reconstructing T_c by using Eq. (24), with κ_2 and κ_4 computed from the results obtained at imaginary chemical potential and then continued to real μ.

TABLE I. Values of the fit parameters for the MF and FRG cases.

	T_c (GeV)	κ_2	κ_4
MF	0.188	0.0311 ± 0.0001	0.0021 ± 0.0001
FRG	0.176	0.0255 ± 0.0005	0.0018 ± 0.0005

Notably, we observe both in the FRG and in the MF case, that the agreement between the two methods is significantly better in the regime of low chemical potential, particularly in the vicinity of vanishing chemical potential. In this region, the phase boundary reconstructed from the data at imaginary μ closely follows the model prediction for real chemical potentials, with discrepancies remaining well within acceptable uncertainties.

However, as the chemical potential increases and approaches the conjectured location of the CEP, the agreement between the reconstruction based on Eq. (24) and the model begins to deteriorate. This happens both in the MF and in the FRG cases. We point out that, while in the MF case we have a precise location of the CEP, the FRG prediction accuracy is limited by the well-known backbending [68]: for high μ and low T, the phase diagram computed within FRG in the LPA exhibits a positive slope, leading to a negative entropy density region. Within this region, the σ expectation value is not monotonous and χ_σ exhibits both a minimum and a maximum, without reaching the divergence condition required for a pure second-order phase transition. Thus, we can only limit the region in which the CEP is located considering the values of μ and T for which we are clearly in a crossover and a first-order phase transition regime.

The difference between the extrapolated result and the actual calculation of the critical line becomes more pronounced the closer we move toward the critical region. The progressive mismatch is expected, as the critical line (24) is based on a reconstruction which is well defined in a neighborhood of $\mu = 0$.

In order to estimate the range of validity of the reconstruction technique from the data at imaginary chemical potential, we compute the relative difference between the actual values of the critical temperature predicted by the model, T_c, and the ones obtained via the reconstruction based on Eq. (24), $T_c^{(\mathrm{fit})}$, that is

$$\varepsilon_{\mathrm{rel}} = \frac{\left| T_c - T_c^{(\mathrm{fit})} \right|}{T_c}. \tag{25}$$

In Fig. 4 we show $\varepsilon_{\mathrm{rel}}$ as a function of μ^2. As expected, the relative error increases with μ^2.

We can use the results in Fig. 4 to extract an effective convergence radius in the μ^2 axis for the extrapolation technique. To this end, we have to fix a threshold value for $\varepsilon_{\mathrm{rel}}$, above which we state that the extrapolation (24) is not convergent. For the sake of concreteness, we fix the threshold value for $\varepsilon_{\mathrm{rel}}$ to 0.10. This leads to the following

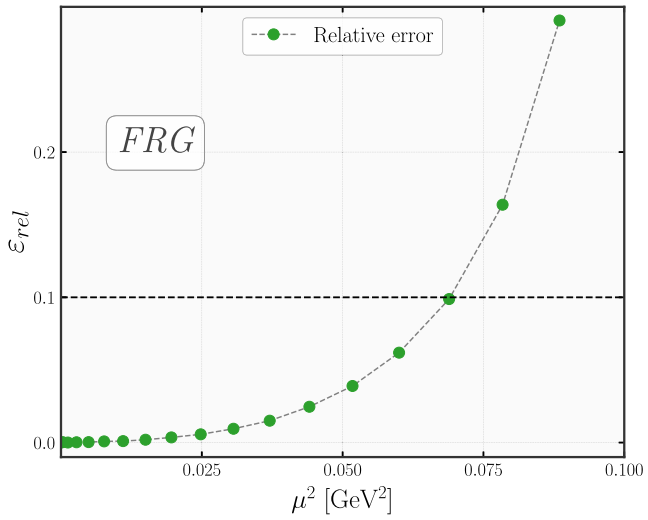


FIG. 4. Relative error $\varepsilon_{\rm rel}$ [see Eq. (25)] of the extrapolated critical temperature in the FRG case. The black horizontal line indicates the threshold of 0.1 in the relative error that we used to estimate the effective convergence radius of the reconstruction technique. For the mean-field case the results are quantitatively similar.

effective convergence radii, $\mu_{\rm conv}$, respectively for the MF and the FRG cases:

$$\mu_{\rm conv} = 0.2820 \text{ GeV}, \qquad \text{MF}, \tag{26}$$

and

$$\mu_{\rm conv} = 0.2625 \text{ GeV}, \qquad \text{FRG}. \tag{27}$$

These results show that the effective convergence radius is similar for both FRG and MF. However, in both cases $\mu_{\rm conv}$ is smaller than the value corresponding to the location of the critical endpoint predicted by the model, and the relative error is of order $\varepsilon_{\rm rel} \approx 1.0$ in the proximity of the CEP. This exercise suggests that the extrapolation from imaginary to real (and large) baryon chemical potential, in order to estimate the location of the critical endpoint, might be taken with a grain of salt.

V. CONCLUSIONS

In this study, we have adopted the hydrodynamic formulation of the FRG applied to the QM model, as an effective chiral model of QCD. We have performed a comparative analysis between the extrapolated critical line from imaginary to real quark chemical potential, μ, and the one actually computed at finite μ. Our objective was to test the standard techniques utilized to reconstruct the phase boundary at real chemical potential starting from data at imaginary chemical potential. To this end, the quark-meson model has been used, both in the mean field and in the FRG approach. For the latter, we have implemented a local-potential approximation. The model provides results for the phase boundary both at real and imaginary μ; hence, we have access to a direct comparison between the real μ results, predicted by the model, and the ones obtained via extrapolation from imaginary μ.

The results of our analysis show that at low chemical potential, particularly in the vicinity of $\mu = 0$, the agreement between the reconstruction from imaginary μ and the model predictions is excellent.

On the other hand, as we move toward higher values of μ, and particularly as we approach the CEP, a progressive deviation between the two approaches becomes evident. The phase boundary reconstructed by the extrapolation from imaginary μ data diverges from the model predictions as μ is increased, indicating difficulty of the extrapolation to capture the nonanalytic behavior associated with criticality.

The trend observed in the comparative analysis underscores both the strengths and the limitations of each approach. The good agreement at low chemical potentials reinforces the validity of the reconstruction method in the crossover regime, while the growing discrepancy near the CEP highlights the need for improved techniques to handle critical dynamics, whether through enhanced lattice methods, better model parametrizations, or hybrid approaches. Importantly, this trend is not merely a technical shortcoming, since it reflects the fundamental challenges involved in describing critical phenomena in QCD. Near the CEP, long-range correlations and nonperturbative effects dominate, and any method not explicitly constructed to handle such dynamics is likely to show signs of breakdown.

It is our opinion that the present work reinforces the usefulness of comparative studies in understanding the strengths and limitations of different theoretical tools used to explore the QCD phase diagram. In particular, while the agreement at low chemical potential supports the methodology of extrapolation from imaginary μ, the discrepancy between the extrapolated critical line and the actual one near the CEP highlights the need for improved techniques, based on first-principle calculations, for finite-density QCD.

Further studies can be carried out investigating the deconfinement QCD phase transition, exploiting the Polyakov-loop enhanced version of the QM model, in which a more precise reconstruction of the imaginary chemical potential dynamic and the RW transition is possible. We intend to asses this problem in a future work.

ACKNOWLEDGMENTS

M. R. acknowledges Bruno Barbieri, Lautaro Martinez, Francesco Acerbi, and John Petrucci for inspiration. This work has been partly funded by the European Union—Next Generation EU through the Research Grant No. P2022Z4P4B "SOPHYA—Sustainable Optimised PHYsics Algorithms: Fundamental Physics to Build an Advanced Society," under the program PRIN 2022 PNRR of the Italian Ministero dell'Università e Ricerca (MUR).

DATA AVAILABILITY

The data that support the findings of this article are openly available at Ref. [69].

[1] K. Fukushima and T. Hatsuda, The phase diagram of dense QCD, Rep. Prog. Phys. **74**, 014001 (2010).

[2] A. Barducci, R. Casalbuoni, S. De Curtis, R. Gatto, and G. Pettini, Chiral symmetry breaking in QCD at finite temperature and density, Phys. Lett. B **231**, 463 (1989).

[3] H. Meyer-Ortmanns, Phase transitions in quantum chromodynamics, Rev. Mod. Phys. **68**, 473 (1996).

[4] T. K. Herbst, J. M. Pawlowski, and B.-J. Schaefer, Phase structure and thermodynamics of QCD, Phys. Rev. D **88**, 014007 (2013).

[5] F. Murgana, V. Greco, M. Ruggieri, and D. Zappalà, Functional renormalization group study of thermodynamic geometry around the phase transition of quantum chromodynamics, Phys. Rev. D **109**, 096017 (2024).

[6] M. A. Stephanov, K. Rajagopal, and E. V. Shuryak, Signatures of the tricritical point in QCD, Phys. Rev. Lett. **81**, 4816 (1998).

[7] F. Wilczek, Application of the renormalization group to a second order QCD phase transition, Int. J. Mod. Phys. A **07**, 3911 (1992); **07**, 6951(E) (1992).

[8] M. Ruggieri, M. Tachibana, and V. Greco, Renormalized vs nonrenormalized chiral transition in a magnetic background, J. High Energy Phys. 07 (2013) 165.

[9] Y. Zhang, D. Zhang, and X. Luo, Experimental study of the QCD phase diagram in relativistic heavy-ion collisions, Nucl. Tech. **46**, 040001 (2023).

[10] G. Roland, K. Safarik, and P. Steinberg, Heavy-ion collisions at the LHC, Prog. Part. Nucl. Phys. **77**, 70 (2014).

[11] N. Armesto, N. Borghini, S. Jeon, and U. A. Wiedemann, *Proceedings, Workshop on Heavy Ion Collisions at the LHC: Last Call for Predictions: Geneva, Switzerland, May 14—June 8, 2007* (IOP Publishing, Bristol, UK, 2008), Vol. 35.

[12] N. Xu (STAR Collaboration), An overview of STAR experimental results, Nucl. Phys. **A931**, 1 (2014).

[13] A. Bazavov *et al.* (HotQCD Collaboration), Chiral and deconfinement aspects of the QCD transition, Phys. Rev. D **85**, 054503 (2012).

[14] C. Ratti and W. Weise, Thermodynamics of two-colour QCD and the Nambu Jona-Lasinio model, Phys. Rev. D **70**, 054013 (2004).

[15] C. Ratti, M. A. Thaler, and W. Weise, Phases of QCD: Lattice thermodynamics and a field theoretical model, Phys. Rev. D **73**, 014019 (2006).

[16] G. Pan and Z. Y. Meng, The sign problem in quantum monte carlo simulations, in *Encyclopedia of Condensed Matter Physics (Second Edition)*, edited by T. Chakraborty (Academic Press, Oxford, 2024), 2nd ed., pp. 879–893.

[17] R. V. Gavai and S. Gupta, Pressure and nonlinear susceptibilities in QCD at finite chemical potentials, Phys. Rev. D **68**, 034506 (2003).

[18] A. Bazavov *et al.*, The QCD equation of state to $\mathcal{O}(\mu_B^6)$ from Lattice QCD, Phys. Rev. D **95**, 054504 (2017).

[19] M. G. Alford, A. Kapustin, and F. Wilczek, Imaginary chemical potential and finite fermion density on the lattice, Phys. Rev. D **59**, 054502 (1999).

[20] R. Bellwied, S. Borsanyi, Z. Fodor, J. Günther, S. D. Katz, C. Ratti, and K. K. Szabo, The QCD phase diagram from analytic continuation, Phys. Lett. B **751**, 559 (2015).

[21] G. Parisi, On complex probabilities, Phys. Lett. **131B**, 393 (1983).

[22] F. Attanasio, B. Jäger, and F. P. G. Ziegler, Complex Langevin simulations and the QCD phase diagram: Recent developments, Eur. Phys. J. A **56**, 251 (2020).

[23] Y. Nambu and G. Jona-Lasinio, Dynamical model of elementary particles based on an analogy with superconductivity. 1, Phys. Rev. **122**, 345 (1961).

[24] Y. Nambu and G. Jona-Lasinio, Dynamical model of elementary particles based on an analogy with superconductivity. II, Phys. Rev. **124**, 246 (1961).

[25] V. Koch, Aspects of chiral symmetry, Int. J. Mod. Phys. E **06**, 203 (1997).

[26] S. Weinberg, *The Quantum Theory of Fields* (Cambridge University Press, Cambridge, England, 1996), Vol. 2.

[27] K. Fukushima and V. Skokov, Polyakov loop modeling for hot QCD, Prog. Part. Nucl. Phys. **96**, 154 (2017).

[28] J. Bernhardt and C. S. Fischer, From imaginary to real chemical potential QCD with functional methods, Eur. Phys. J. A **59**, 181 (2023).

[29] M. E. Peskin and D. V. Schroeder, *An Introduction to Quantum Field Theory* (Westview Press, Addison-Wesley, Reading, MA, 1995), p. 842.

[30] M. Gell-Mann and M. Levy, The axial vector current in beta decay, Nuovo Cimento **16**, 705 (1960).

[31] F. Murgana, A. Koenigstein, and D. H. Rischke, Reanalysis of critical exponents for the O(N) model via a hydrodynamic approach to the functional renormalization group, Phys. Rev. D **108**, 116016 (2023).

[32] K. S. Jeong, F. Murgana, A. Dash, and D. H. Rischke, Functional Renormalization Group analysis of the quark-condensation pattern on the Fermi surface: A simple effective-model approach, arXiv:2407.13589.

[33] A. Koenigstein, M. J. Steil, N. Wink, E. Grossi, J. Braun, M. Buballa, and D. H. Rischke, Numerical fluid dynamics for FRG flow equations: Zero-dimensional QFTs as numerical test cases—Part I: The $o(n)$ model, arXiv:2108.02504.

[34] J. Braun, M. Leonhardt, and J. M. Pawlowski, Renormalization group consistency and low-energy effective theories, SciPost Phys. **6**, 56 (2019).
[35] J. Stoll, N. Zorbach, A. Koenigstein, M. J. Steil, and S. Rechenberger, Bosonic fluctuations in the $(1+1)$-dimensional Gross-Neveu(-Yukawa) model at varying μ and T and finite N, arXiv:2108.10616.
[36] U. Ellwanger, Flow equations for N point functions and bound states, Z. Phys. C **62**, 503 (1994).
[37] C. Wetterich, Exact evolution equation for the effective potential, Phys. Lett. B **301**, 90 (1993).
[38] T. R. Morris, On truncations of the exact renormalization group, Phys. Lett. B **334**, 355 (1994).
[39] M. Reuter and C. Wetterich, Effective average action for gauge theories and exact evolution equations, Nucl. Phys. **B417**, 181 (1994).
[40] J. M. Pawlowski, Aspects of the functional renormalisation group, Ann. Phys. (N.Y.) **322**, 2831 (2007).
[41] P. Kopietz, L. Bartosch, and F. Schütz, *Introduction to the Functional Renormalization Group* (Springer, Berlin, Heidelberg, 2010), Vol. 798.
[42] N. Dupuis, L. Canet, A. Eichhorn, W. Metzner, J. M. Pawlowski, M. Tissier, and N. Wschebor, The nonperturbative functional renormalization group and its applications, Phys. Rep. **910**, 1 (2021).
[43] J. Berges, N. Tetradis, and C. Wetterich, Nonperturbative renormalization flow in quantum field theory and statistical physics, Phys. Rep. **363**, 223 (2002).
[44] C. Wetterich, Average action and the renormalization group equations, Nucl. Phys. **B352**, 529 (1991).
[45] J. M. Pawlowski, Aspects of the functional renormalisation group, Ann. Phys. (N.Y.) **322**, 2831 (2007).
[46] D. F. Litim, Critical exponents from optimized renormalization group flows, Nucl. Phys. **B631**, 128 (2002).
[47] D. F. Litim, Optimized renormalization group flows, Phys. Rev. D **64**, 105007 (2001).
[48] L. Canet, B. Delamotte, D. Mouhanna, and J. Vidal, Optimization of the derivative expansion in the nonperturbative renormalization group, Phys. Rev. D **67**, 065004 (2003).
[49] T. R. Morris, The exact renormalization group and approximate solutions, Int. J. Mod. Phys. A **09**, 2411 (1994).
[50] B. Bergerhoff and C. Wetterich, Effective quark interactions and QCD propagators, Phys. Rev. D **57**, 1591 (1998).
[51] J. A. Adams, J. Berges, S. Bornholdt, F. Freire, N. Tetradis, and C. Wetterich, Solving nonperturbative flow equations, Mod. Phys. Lett. A **10**, 2367 (1995).
[52] E. Grossi and N. Wink, Resolving phase transitions with discontinuous Galerkin methods, SciPost Phys. Core **6**, 071 (2023).
[53] E. Grossi, F. J. Ihssen, J. M. Pawlowski, and N. Wink, Shocks and quark-meson scatterings at large density, Phys. Rev. D **104**, 016028 (2021).
[54] B. Delamotte, An introduction to the nonperturbative renormalization group, Lect. Notes Phys. **852**, 49 (2012).
[55] D. F. Litim, Optimized renormalization group flows, Phys. Rev. D **64**, 105007 (2001).
[56] D. F. Litim, Critical exponents from optimised renormalisation group flows, Nucl. Phys. **B631**, 128 (2002).
[57] N. Zorbach, A. Koenigstein, and J. Braun, Functional renormalization group meets computational fluid dynamics: RG flows in a multi-dimensional field space, arXiv:2412.16053.
[58] A. Koenigstein, L. Pannullo, S. Rechenberger, M. J. Steil, and M. Winstel, Detecting inhomogeneous chiral condensation from the bosonic two-point function in the $(1+1)$-dimensional Gross–Nneveu model in the mean-field approximation, J. Phys. A **55**, 375402 (2022).
[59] A. Kurganov and E. Tadmor, New high-resolution central schemes for nonlinear conservation laws and convection–diffusion equations, J. Comput. Phys. **160**, 241 (2000).
[60] J. W. Thomas, *Numerical Partial Differential Equations: Conservation Laws and Elliptic Equations* (Springer, New York, 1999).
[61] E. Bladé, M. Gómez-Valentín, J. Dolz, J. Aragón-Hernández, G. Corestein, and M. Sánchez-Juny, Integration of 1d and 2d finite volume schemes for computations of water flow in natural channels, Adv. Water Resour. **42**, 17 (2012).
[62] G.-S. Jiang and E. Tadmor, Nonoscillatory central schemes for multidimensional hyperbolic conservation laws, SIAM J. Sci. Comput. **19**, 1892 (1998).
[63] A. Koenigstein, M. J. Steil, N. Wink, E. Grossi, J. Braun, M. Buballa, and D. H. Rischke, Numerical fluid dynamics for FRG flow equations: Zero-dimensional QFTs as numerical test cases. I. The O(N) model, Phys. Rev. D **106**, 065012 (2022).
[64] A. Koenigstein, M. J. Steil, N. Wink, E. Grossi, and J. Braun, Numerical fluid dynamics for FRG flow equations: Zero-dimensional QFTs as numerical test cases. II. Entropy production and irreversibility of RG flows, Phys. Rev. D **106**, 065013 (2022).
[65] F. Ihssen, F. R. Sattler, and N. Wink, Numerical RG-time integration of the effective potential: Analysis and benchmark, Phys. Rev. D **107**, 114009 (2023).
[66] K. Morita, V. Skokov, B. Friman, and K. Redlich, Role of mesonic fluctuations in the Polyakov loop extended quark-meson model at imaginary chemical potential, Phys. Rev. D **84**, 074020 (2011).
[67] S. Borsanyi, Z. Fodor, J. N. Guenther, R. Kara, S. D. Katz, P. Parotto, A. Pasztor, C. Ratti, and K. K. Szabo, QCD crossover at finite chemical potential from lattice simulations, Phys. Rev. Lett. **125**, 052001 (2020).
[68] R.-A. Tripolt, J. Weyrich, L. von Smekal, and J. Wambach, Fermionic spectral functions with the functional renormalization group, Phys. Rev. D **98**, 094002 (2018).
[69] F. Murgana, Supplementary data for "Assessing the reconstruction of the critical line in the QCD phase diagram from imaginary to real chemical potential", https://drive.google.com/drive/folders/1Puc88P5GDnEzwTJhbuKrnOpaB2hqtdX9.